Quasi-liquid grain boundary conductivity in solid electrolyte candidate lithium imide

Jeremy P. Lowen[1], Teresa Insinna[2], Tharigopala V. Beatriceveena[1], Mark P. Stockham[1], Bo Dong[1], Sarah J. Day[3], Clare P. Grey[2], Emma Kendrick[4], Peter R. Slater[1], Paul A. Anderson[1] and Joshua W. Makepeace[1*]

[1]School of Chemistry, University of Birmingham, Edgbaston, United Kingdom, B15 2TT
[2]Yusuf Hamied Department of Chemistry, University of Cambridge, Cambridge, United Kingdom, CB2 1EW
[3]I11 Beamline, Diamond Light Source, Didcot, United Kingdom, OX11 0QX
[4]School of Materials and Metallurgy, University of Birmingham, United Kingdom, B15 2TT

All-solid-state batteries utilising a Li-metal anode have long promised to be the next-generation of high-performance energy storage device, with a step-change in energy density, cycling stability and cell safety touted as potential advantages compared to conventional Li-ion battery cells. A key to enabling this technology is the development of solid-state electrolytes with the elusive combination of high ionic conductivity, wide electrochemical stability and the ability to form a conductive and stable interface with Li metal. Presently, oxide and sulfide-based materials, particularly garnet and argyrodite-type structures, have proved most promising for this application. However, these still suffer from a number of challenges, including resistive lithium metal interfaces, poor lithium dendrite suppression (at high current density) and low voltage stability. Here we report the first application of lithium imide, an antifluorite-structured material, as a solid electrolyte in a Li-metal battery. Low-temperature synthesis of lithium imide produces promising Li-ion conductivity, reaching > 1 mS cm^{-1} at 30 ˚C using a modest post-synthetic mechanochemical treatment, as well as displaying at least 5 V stability *vs* Li$^+$/Li. *In situ* electrochemical operation of lithium imide with Li-metal electrodes reveals a 1000-fold increase in its measured ionic conductivity, whilst appearing to remain an electronic insulator. It is postulated that stoichiometry variation at the grain boundary leads to a highly disordered quasi-liquid state, facilitating this conductivity improvement. Furthermore, the material is shown to possess impressive stability under high current density conditions (70 mA cm^{-2}) as well as the ability to operate in Li-metal battery cells. These results not only highlight the promising performance of lithium imide, but also its potential to be the basis for a new family of antifluorite based solid electrolytes.

The growing demand for batteries with high power and greater energy density is driving the push for adopting lithium metal anodes in the next generation of Li-ion battery technology.[1,2] This transition is however hindered by a number of challenges including lithium dendrite propagation, the formation of 'dead' lithium, and chemical incompatibility with current liquid electrolytes, which leads to uncontrolled solid electrolyte interphase (SEI) growth during cycling.[1–3] A key strategy towards resolving these issues is to replace organic liquid electrolytes with a solid ceramic or polymer alternative forming a so-called all solid-state battery (ASSB).[4–6] Employing a solid-state electrolyte (SSE) could offer chemical compatibility with lithium metal, provide a mechanical barrier to dendrite growth, enable the use of future high-voltage cathodes, and address the safety concerns associated with current liquid electrolytes.[4,7] Finding a suitable SSE material is not, however, straightforward; the performance of the electrolyte must meet a number of strict requirements including:

- High ionic conductivity of at least 0.1 mS cm^{-1} at room temperature. [7,8]
- Electronically insulating. [7,8]
- A wide electrochemical stability window comparable to or greater than that of a conventional liquid electrolyte (up to ~4.2 V vs Li$^+$/Li) with a reduction potential close to that of lithium metal (0 V vs Li$^+$/Li).[7–9]
- Low resistance interfaces with both lithium metal and the relevant cathode.
- Lightweight, cheap, and easily accessible through commercially viable synthesis routes.

To date, numerous ceramic material types (ranging from oxides to sulfides) with a variety of structures (e.g. Garnet, LISICON, Argyrodite) have been researched for this application, though the majority have yet to reach the market.[10–15] Even the most extensively researched materials, where impressively high ionic conductivities have been recorded, still have significant challenges to their practical application. Oxide-based materials, such as lithium garnets, are often mechanically hard and form surface lithium carbonates, consequently exhibiting poor wettability with lithium metal and highly resistive interfaces.[16,17] Sulfide-based materials, whilst softer, display a low upper-voltage stability and are extremely moisture sensitive.[18] Fluorite-structured oxides and fluorides have long been researched in the context of solid oxide fuel cells and solid-state fluoride batteries, due to their high ambient temperature anionic conductivity.[19–23] Despite this, comparatively little attention has been paid to corresponding lithium antifluorite materials for Li-ion solid electrolyte application, aside from lithium nitride

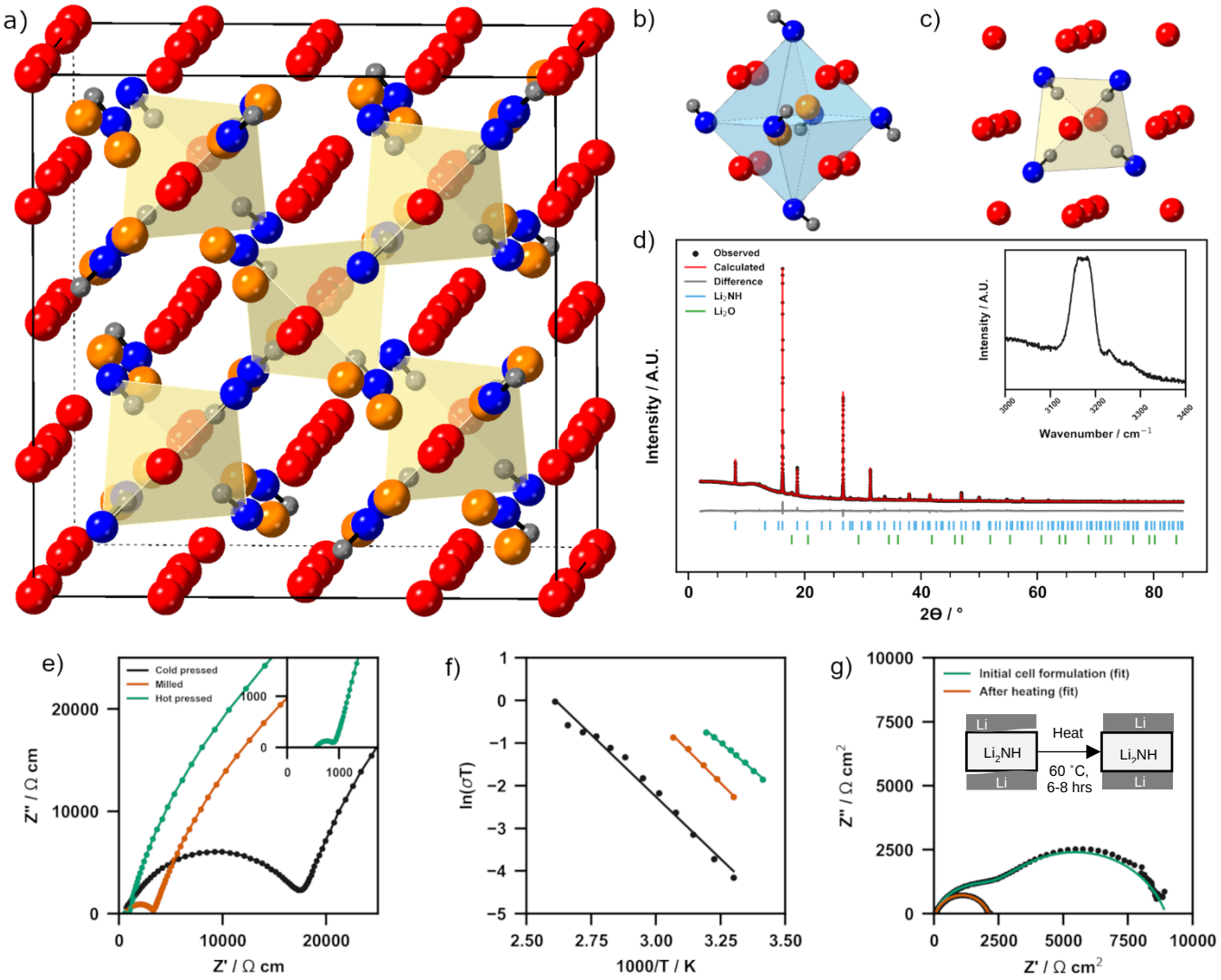

Figure 1: a) $Fd\bar{3}m$ structure of stoichiometric Li_2NH with tetrahedral Li ions shown in red, interstitial Li ions in orange, N in blue and H in grey. b) Octahedral hole occupied by interstitial Li-ions c) Tetrahedral coordination of local N-H bonds towards vacancy left by Li displacement. d) Powder XRD pattern including experimental data and Rietveld fit of Li_2NH with inset Raman spectra. e) Nyquist impedance spectra of Au|Li_2NH|Au cells at 30 ˚C with different pellet preparation strategies. f) Arrhenius plots of each Au|Li_2NH|Au cell. g) Nyquist impedance spectra of a Li|Li_2NH|Li cell before and after simple heat treatment. A schematic of proposed interface stabilisation is shown.

chloride systems and recent phosphorus-doped lithium sulphide.[24–26]

Lithium imide (Li_2NH), a nitrogen-based complex metal hydride with an antifluorite-type structure, has previously been explored for its readily-reversible hydrogen storage reaction and impressive catalytic activity for ammonia decomposition.[27–30] A key characteristic driving the performance of this material in these applications is its high reported lithium-ion conductivity (10^{-5}–10^{-4} S cm^{-1}), yet only one study has investigated the electrochemical characteristics of the material.[31–34] This may relate to initial suggestions of a narrow operational voltage range, though these were not experimentally verified. Indeed, subsequent studies of lithium imide point towards a promising set of properties: it is thermally stable up to 600 ˚C, has an apparently wide electrochemical stability window and ^{7}Li NMR data suggest the main charge carrier to be Li^+, signifying that Li_2NH is likely electronically insulating.[35,36] Molecular dynamics simulations have indicated that Li^+ diffuses via an interstitialcy-type mechanism, intrinsically linked with the rotation of N-H bonds within the structure.[37,38] Although moisture sensitive, Li_2NH can reportedly be formed in as little as 10 minutes at 210 ˚C and is composed of largely abundant and lightweight elements, making it more suitable for low cost and high energy density systems as compared to other archetypal SSEs.[39] Herein we demonstrate the significant potential of Li_2NH as a SSE, with a new highest recorded bulk ionic conductivity for the material (> 1 mS cm^{-1} at RT), wide electrochemical stability window (≥ 5 V) and excellent high current density operational capability (at up to 70 mA cm^{-2}). We demonstrate that *in situ* operation of a Li_2NH SSE using a Li-metal symmetric cell induces a metastable further increase in the ionic conductivity (> 10 mS cm^{-1}) without bulk structural changes to the material, indicating activation of fast grain boundary diffusion. Operation of hybrid solid-state batteries utilising a

Li_2NH SSE and Li-metal anode is also achieved with two separate cathode materials ($LiFePO_4$ and TiS_2). This material therefore represents a promising new system for achieving high-performance solid-state Li-metal batteries.

Structure and synthesis

Lithium imide is widely accepted to adopt a cubic antifluorite-based structure, although there are differing reports as to whether at room temperature this is a simple antifluorite cell with disordered N-H orientations ($Fm\bar{3}m$ symmetry) or a larger superstructure (e.g. $Fd\bar{3}m$ symmetry, Figure 1a) with ordered displacement of Li-ions into octahedral holes (Figure 1b) and tetrahedral coordination of the lithium vacancy by N-H groups (Figure 1c).[40–43] In essence, this structure represents an ordered Frenkel defect variation on the classic antifluorite structure. Given the propensity for Li_2NH to form antifluorite-structured $Fm\bar{3}m$ symmetry solid solutions with other N-H based materials, it is unlikely that there are two room temperature polymorphs of Li_2NH. Instead, experimental reports of the disordered structure for stoichiometric Li_2NH are much more likely off-stoichiometry due to amide (NH_2^-), nitride (N^{3-}) or hydride (H^-) impurities associated with the synthesis method. [31,44–46] Multiple molecular dynamics and density functional theory simulations investigating the structure of Li_2NH support this assertion, indicating that stoichiometric Li_2NH should take the ordered superstructure at room temperature.[37,47–50] It should be noted that previous reports of the Li-ion conductivity of Li_2NH have almost exclusively been from samples with this disordered structure and not therefore stoichiometric Li_2NH. The synthesis of Li_2NH was achieved using the solid-state reaction of Li_3N with $LiNH_2$ first reported by Hu and Ruckenstein.[39] The powder X-ray diffraction pattern of Li_2NH is displayed in Figure 1d. The peak at 6.9˚ corresponds to the (111) reflection characteristic of the $2a\times2a\times2a$ antifluorite superstructure of stoichiometric Li_2NH. Rietveld analysis was performed using a previously reported $Fd\bar{3}m$ structure to fit the Li_2NH phase.[43]

The inset Raman spectrum displays a broad peak at approximately 3180 cm^{-1} corresponding to the linear imide stretch and is consistent with previously reported spectra.[34,45,51] Two minor peaks at 3240 cm^{-1} and 3275 cm^{-1} are likely indicative of very minor levels of residual amide ions left in the solid solution.[45] Compared to other solid electrolyte preparations, the synthesis conditions for Li_2NH are very mild. For example, typical garnet-type oxides often require multiple firings at temperatures > 900 ˚C to complete their synthesis, whilst in this synthesis the sample is calcined in a single step at only 325 ˚C.[52]

Ionic and electronic conductivity

The ionic conductivity of as-prepared, cold pressed Li_2NH was determined at 30 ˚C *via* electrochemical impedance spectroscopy (EIS) on an Au|Li_2NH|Au cell. The Nyquist plot for this measurement is displayed in Figure 1e and the full Nyquist plot with equivalent circuit model is found in Supplementary Figure 1 (results of fitting found in Supplementary Table 1). One semi-circle may be observed which is assigned to the impedance associated with the combined bulk/grain boundary transport, followed by a spike observed at high frequency, which is characteristic of Li_2NH-Au interface charging. This blocking behaviour is a good indication that Li_2NH is a purely ionic conductor. The conductivity was calculated using the total bulk/grain boundary contribution and was found to be 0.054 mS cm^{-1}. This is of the same order as the previous literature for this phase.[34] A potential detriment to the total conductivity of this system is likely the porosity of the cold-pressed pellet which had a relative density of 76.5%. The electronic conductivity and transference numbers of Li_2NH were determined using DC polarisation on the same Au|Li_2NH|Au held at 40 ˚C (Supplementary Figure 2). The electronic conductivity was calculated to be 1.2 nS cm^{-1} whilst t_i was found to be 0.998, confirming that all charge transfer may be attributed to ionic movement and that Li_2NH is an electronic insulator.

Given that the ionic conductivity for cold-pressed Li_2NH does not meet the threshold for SSE application we have pursued further pellet preparation strategies to improve this property. Figure 1e displays Nyquist plots of these other preparations at 30 ˚C. Full Nyquist plots with equivalent circuit fitting can also be found in Supplementary Figure 1 (fitting results in Supplementary Table 1). Similar to cold-pressed Li_2NH, one semi-circle and spike can be observed for each preparation. A pre-treatment of Li_2NH powder through low-energy ball milling before cold pressing was found to improve the conductivity to 0.34 mS cm^{-1}, whilst retaining a similar pellet relative density of 77%. This improvement in conductivity is likely due to improved grain boundary diffusion, potentially through inducing disorder from milling. Similar effects from milling have been reported for fluorite-based materials, however, to our knowledge this is the first report of this behaviour for an antifluorite material.[53] Hot pressing Li_2NH at 325 ˚C for just one hour has an even greater effect than milling, improving the conductivity to 1 mS cm^{-1} (Figure 1e inset), the highest recorded conductivity for this material at room temperature. These improvements are likely due to morphological effects as well as a gain in pellet relative density to 85% during hot pressing. Arrhenius plots for the conductivity of all three pellet preparations across a range of temperatures are shown in Figure 1f. The activation energy for lithium diffusion was calculated to be 0.50(2)

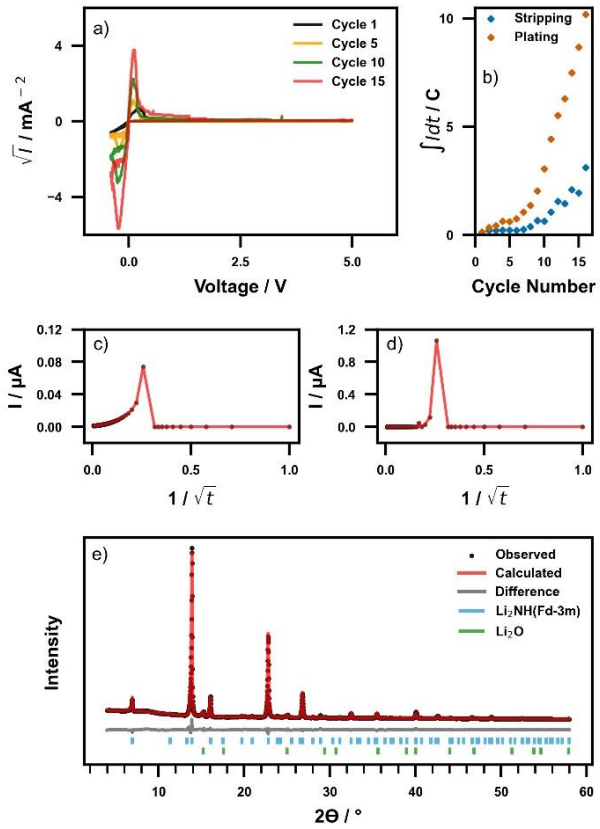

Figure 2: a) Cyclic voltammograms of a Li|Li_2NH|Steel cell at 40˚C. b) Integrated current vs cycle number for stripping and plating. c) DC polarisation taken c) before and after d) cycling. e) Post-CV (16 completed cycles) powder XRD pattern of material after cell disassembly.

eV for cold pressed Li_2NH, 0.52(2) eV for milled + cold pressed and 0.44(1) eV for hot pressed Li_2NH. These values are of the order of previously reported values for Li_2NH.[32–34] The lower activation energy for hot pressed Li_2NH is likely a reflection of improved grain boundary diffusion and the lower porosity of the pellet. Given the conductivity gains with these relatively simple physical treatments, it is likely that further optimisation of the sample morphology will yield additional improvements.

Li-metal interface

Figure 1g displays Nyquist plots for a Li|Li_2NH|Li cell at 30 ˚C before and after heat treatment. Upon initial construction of the cell a large interfacial impedance is observed (~ 3308 Ω cm^2) between the Li_2NH and Li-metal. However, a simple heat treatment of just 60 ˚C for 6-8 hours largely eliminates this interfacial resistance (~ 47 Ω cm^2). Equivalent circuit fitting results of these spectra may be found in Supplementary Figure 3 and Supplementary Table 2. The conductivity of the cell post heat-treatment is found to be in good agreement with Au|Li_2NH|Au data at 0.059 mS cm^{-1}. Post thermal treatment X-ray diffraction analysis (Supplementary Figure 4) displays that no crystalline impurities are formed during this procedure, indicating that this process is likely to be either a mechanical wetting of the interface or a surface-confined reaction which improves conductivity. A proposed mechanical interface formation process is displayed as a schematic in Figure 1g.

Electrochemical stability

The electrochemical stability of Li_2NH was assessed *via* cyclic voltammetry (CV) between -0.5 V and 5 V *vs* Li/Li^+ on a Li|Li_2NH|Steel cell where the Li-metal electrode was melded to the Li_2NH pellet *via* the method used above. No extra pressure was applied to the cell beyond the spacer and spring used in fabrication. The cyclic voltammograms for this measurement are displayed in Figure 2a. Anodic and cathodic currents corresponding to lithium stripping (positive current, Li → $Li^+ + e^-$) and lithium plating (negative current, $Li^+ + e^-$ → Li) can be observed near 0 V. No currents corresponding to electrolyte decomposition were observed over 16 cycles, indicating that Li_2NH is electrochemically stable across the measured voltage range. However, it can be observed that the currents corresponding to lithium stripping/plating increase with increasing cycle number. This has previously been ascribed to an improving interfacial morphology between the SSE and Li-metal during cycling, however, it is also possible that the ionic conductivity of the cell is improving through another mechanism, allowing more lithium to diffuse each cycle. [54]

The rate of increase in plating/stripping currents with cycle number follows two regimes, as displayed in Figure 2b. Initially (cycles 1–7), the proportion of lithium stripped/plated increases slowly, followed by a rapid increase (cycles 7–16). In this second regime, the ratio of stripping peak area to plating peak area appears to stabilise (Supplementary Figure 5). By analysing the difference in the total amount of lithium stripped and plated it was found that 5.2% more lithium is plated than stripped (calculated as a percentage of the number of moles of lithium in Li_2NH). This discrepancy may be explained either by the formation of dead lithium as a result of loss of contact at the Li-Li_2NH interface or may be representative of a chemical change in the cell. A loss of lithium could for instance indicate the formation of an imide-amide phase ($Li_{2-x}NH_{1+x}$) which are well known and exist over a wide stoichiometry range where

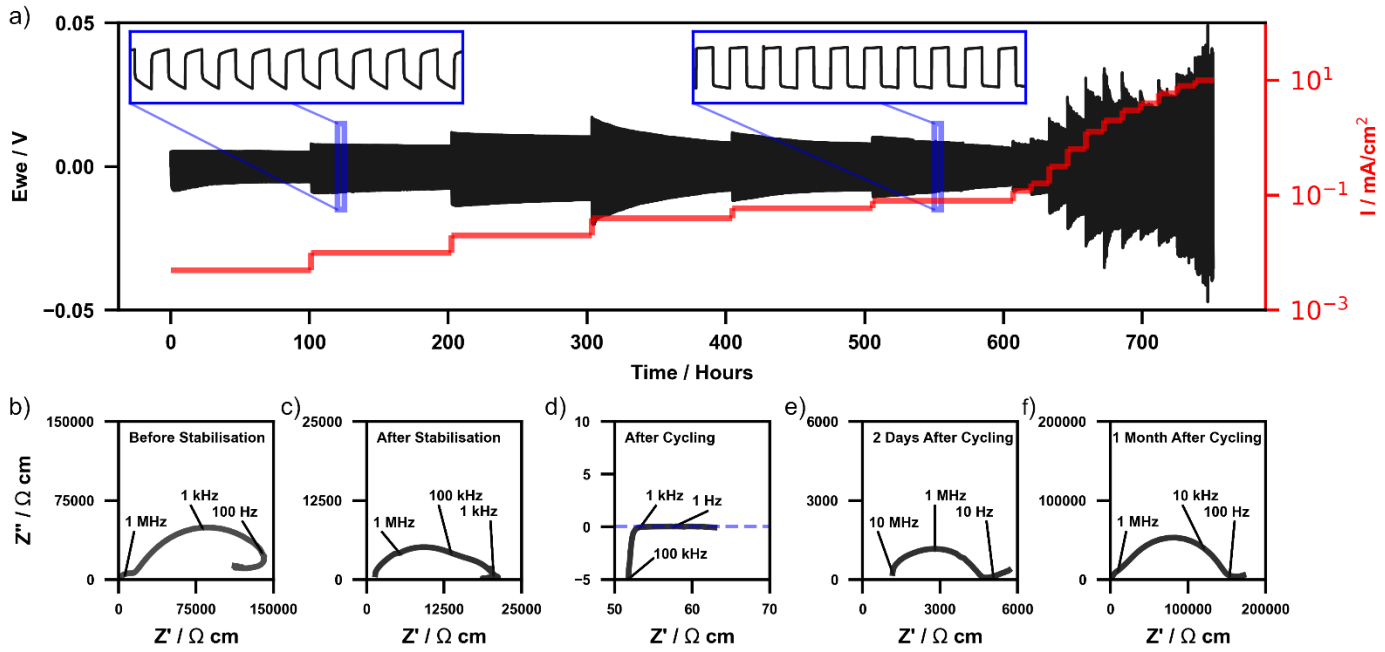

Figure 3: a) Lithium stripping and plating data of a Li|Li_2NH|Li cell cycled at 40 ˚C at various increasing current densities. The positive and negative currents are not displayed to not obscure the voltage data, a line indicating the set current density is instead used alternating between positive and negative currents in 15-minute intervals. Nyquist plots of cell b) before interface stabilisation, c) after interface stabilisation, d) immediately post-cycling, e) 2 days after cycling, and f) 1 month after cycling.

up to two-thirds of imide ions can be replaced by NH_2^- within the Li_2NH structure.[31]

It is clear that there is a mechanical and/or chemical interaction between lithium metal and Li_2NH. To probe this interaction a DC polarisation experiment using a voltage of 0.5 V was undertaken both before and immediately (within 2 minutes) after the CV experiment, with data displayed in Figure 2c and 2d. The plateau currents imply an electronic conductivity pre-CV and post-CV of 0.45 nS cm^{-1} and 54 nS cm^{-1}, respectively (see Supplementary Figure 6), indicating that the cell is still electronically insulating with a small increase, possibly reflecting lithium penetration reducing the effective thickness of the pellet. This is also reflected in the calculated transference numbers pre- and post-CV, where t_i is found to be 0.981 and 0.999 respectively. Post-CV there is a far greater spike in current upon initial polarisation (74 nA pre-CV to 1.06 mA post-CV) and a much faster relaxation period compared to the pre-CV measurement. Fitting of both sets of data using exponential decay functions revealed a decrease in this current relaxation period of 4.48(6) s pre-CV to 2.28(1) s post-CV (Supplementary Figure 6 and Supplementary Table 3). Given that this spike is typically associated with the initial movement of ionic charge carriers upon polarisation this interaction is therefore indicated to result in an overall increase in the ionic conductivity of the cell. Cell disassembly and subsequent X-ray diffraction measurement (Figure 2e) again indicates no change in the bulk structure of Li_2NH, nor formation of impurities detected during this process. Given the lack of apparent bulk chemical change, several possible mechanisms for this increased conductivity are conceivable:

1. An electrochemically driven morphological process potentially resulting in pellet densification.
2. An *in situ* reversible phase transition of Li_2NH to a simpler antifluorite cell ($Fd\bar{3}m \rightarrow Fm\bar{3}m$) resulting in increased ionic diffusion as theorised in computational studies.[50]
3. Grain boundary/particle surface stoichiometry variation on a local scale undetectable *via* a bulk technique such as diffraction.

It is possible that the discrepancy in lithium stripped and plated reflects a change in the lithium content at the surface or grain boundaries of Li_2NH particles. Fluorite-type anionic conductors have been found to have increased ionic mobility through the grain boundaries due to stoichiometry variation.[53,55,56] Furthermore, recent *ab initio* simulations of a Li_2NH surface catalysing ammonia decomposition with subsequent formation of a non-stoichiometric imide-amide particle surface results in a highly disordered, quasi-liquid surface, where fast-ionic diffusion is extremely plausible.[57] While these simulations were at 500 °C, it is conceivable that similar particle surface stoichiometry variation under electrochemical conditions might induce an analogous effect, resulting in 'ionic highways' along the grain boundaries of Li_2NH particles.

Lithium stripping and plating

To assess the long-term stability of Li_2NH in contact with a lithium metal anode under battery operating conditions and further understand the interaction between the two materials, lithium stripping and plating experiments (S&P) under constant current conditions

were conducted on a Li|Li_2NH|Li cell. Figure 3a displays the time-dependent voltage profile of the cell at 40 ˚C cycled for 200 cycles at 5, 10, 20, 40 and 80 μA cm^{-2} and then for 25 cycles at increasing current densities up to 10 mA cm^{-2}. An inset image displays a zoomed-in view of several voltage profiles at a current density of 10 μA cm^{-2} and 80 μA cm^{-2}. Under these conditions Li_2NH is shown to undergo over 750 hours of cycling (> 1250 cycles) without a dramatic drop in current that might indicate a hard short-circuit. Upon each current density increase a corresponding increase in voltage is also observed, again indicating no short circuit. However, during 40 μA cm^{-2} cycling, a slow decrease in the voltage profile is observed resulting in a lower stable cycling voltage. This voltage drop corresponds to the overall cell resistance reducing each cycle and is also observed at higher current densities at accelerated rates. Whilst this could be the result of slow dendrite penetration it is also consistent with observations from the CV experiments (Figure 2) that ionic conductivity increases whilst cycling with a Li-metal electrode.

EIS measurements (Figure 3b-f) were completed both before and after S&P to understand further the effect on conductivity whilst cycling with Li-metal (Bode plots and phase angle data of each EIS measurement are included in Supplementary Figure 7). Figure 3b and 3c show the Li|Li_2NH|Li cell Nyquist plots before interface stabilisation and post-thermal treatment respectively. Before stabilisation two diffusion mechanisms are observed, one at 10^3-10^4 Hz ascribed to interfacial diffusion with Li-metal, and another at ~10^7 Hz (with a phase angle of -45˚) assigned to bulk diffusion. After stabilisation the interfacial component disappears. In both cases a low frequency inductive loop is observed. The exact cause of this remains ambiguous however these have been ascribed in other systems to interfacial stoichiometry variation and may reflect a similar effect at the surface of the Li_2NH particles.[58,59] Figure 3d displays the Nyquist plot of the cell immediately after cycling where a decrease in cell impedance by a factor of ~1000 corresponding to a conductivity of > 10 mS cm^{-2} is observed. The high frequency bulk diffusion process observed before cycling is no longer present, replaced by a process with a phase angle of 90˚. Minimal capacitive behaviour is seen (Supplementary Figure 8), indicating that lithium is able to move freely through the cell.[60] Combining these two observations points towards the change observed being surface related. The conductivity calculated post-cycling is on the order of the best solid-state ionic conductors known to date, however, the exact nature of this improvement is enigmatic. Figure 3e and 3f display EIS measurements on the same cell after set periods of time at rest. Over this time the cell is observed to display relaxation/recovery behaviour. This is reflected in both an observed recovery of cell resistance as well as in the phase angle data, where two days after cycling the high-frequency angle returns to around 45° indicating a bulk diffusion limited process. After one month, the low frequency diffusion process assigned to a Li_2NH|Li interfacial component returns, whereby the impedance spectrum is comparable to that of prior to stabilisation. This implies a dynamic and metastable interfacial process underpins the increased conductivity observed. Repeat experiments performed on separate cells show similar conductivity improvement and corresponding recovery behaviour (Supplementary Figure 9). Synchrotron X-ray diffraction of the post-cycled material shows again no change to the bulk structure nor appreciable formation of impurities (Supplementary Figure 10).

Given the limitations of the structural changes which can be ascertained from average structure measurements, solid state NMR spectroscopy was employed as a means of assessing local changes in the material. Supplementary Figure 11 displays ^{7}Li and ^{1}H spectra for pristine and post-cycled Li_2NH. The ^{7}Li NMR spectrum of the pristine Li_2NH consists of a sharp Lorentzian line centred at 3.30 ppm with an underlying broader component centred at 3.40 ppm, suggesting two separate Li ion environments, one more mobile than the other. The post-cycled sample displays a shift in the broader component to 3.03 ppm, indicative of a minor change in this environment post cycling and potentially minor stoichiometry variation. It should be noted that changes in signal intensity between the two materials remain inconclusive due to measurements having been run at different magnetic fields (the cycled sample having therefore experienced greater polarisation) and on different probes (with different *Q*-factors). However, qualitatively we observe a drop in the ^{7}Li signal intensity between the pristine and cycled material, perhaps suggesting Li loss. A change is also observed in the ^{1}H NMR spectra where the pristine sample shows a variety of environments associated with the NH_x groups: one at −4.35 ppm which is likely the imide groups, one at −1.53 ppm which may be residual amide groups as discussed above, and some very low intensity resonances at 3.97 ppm, which are in the chemical shift region of saline hydrides.[61] Post cycling the main peak shifts to − 5.13 ppm and the second peak to − 2.28 ppm again indicating stoichiometry variation compared to the pristine sample (discussed in further detail below). Furthermore, the echo delay in the Hahn echo pulse sequence can be increased to filter out fast relaxing components (i.e. having a short transverse, T_2, relaxation time). Such T_2-filtered ^{1}H spectra (Supplementary Figure 12) highlight a higher proportion of less mobile hydrogen environments in the post-cycled sample. Both amide and hydride anions are expected to be less mobile than the free rotation of the imide group within Li_2NH, suggesting the presence of one/both of these anions in low quantities. Whilst these data indicate that the observed process is potentially non-stoichiometric in its nature, the metastability

demonstrated by the observed recovery behaviour limits the insight offered by *ex-situ* analysis on the mechanism of the conductivity increase. Therefore, *in situ* diffraction and NMR measurements were performed to gain temporal resolution.

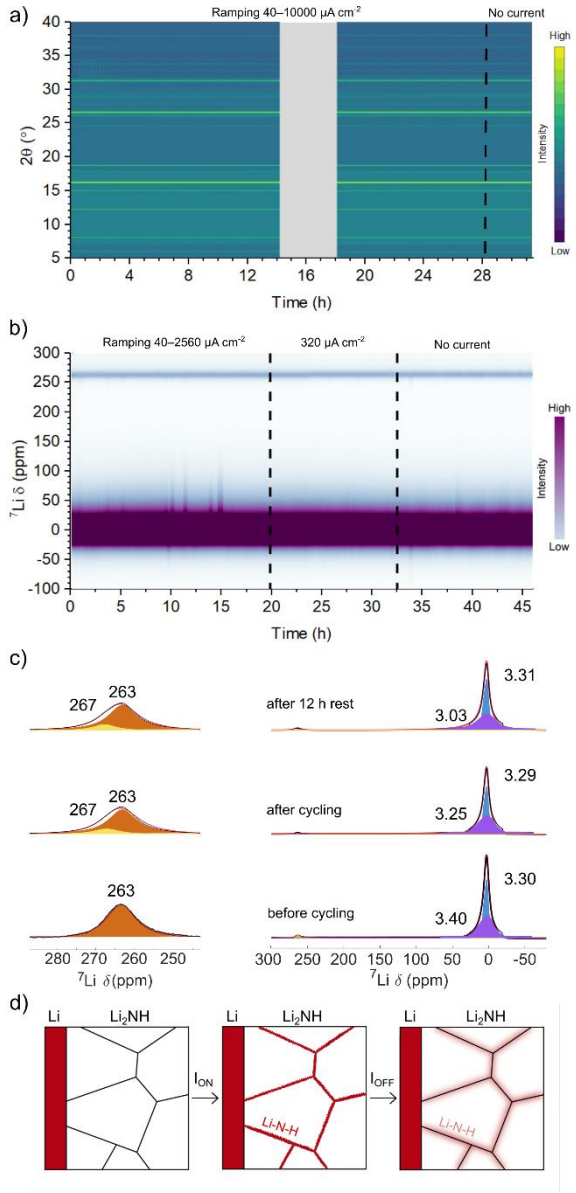

Figure 4: Contour plots of a) synchrotron X-ray diffraction data and b) ^{7}Li SS non-spinning NMR spectra from Li|Li_2NH|Li coin cells during lithium stripping and plating at the indicated current densities, with c) key SSNMR spectra fitted with a CSA static model. A schematic of the proposed mechanism of enhanced grain boundary Li-ion conduction through non-stoichiometric Li-N-H phase formation at grain boundaries, and subsequent diffusion into the grains is shown in d).

In-situ X-ray diffraction and solid-state ^{7}Li NMR

An accelerated S&P experiment with *in situ* synchrotron diffraction was carried out to assess bulk structure behaviour during cycling, particularly with regard to potential metastable phases or stoichiometry variation. In this case cycling was started at 40 μA cm^{-2} and doubled every 3 hours up to 10 mA cm^{-2}. The electrochemical data for this experiment are displayed in Supplementary Figure 13 with a contour plot of the observed diffraction data at each indicated current density displayed in Figure 4a (example diffraction pattern shown in Supplementary Figure 14). Again, despite the accelerated timescale of this experiment, there is no sudden and sustained drop in voltage to indicate a short circuit and a similar lowering of resistance is observed. The diffraction data display no change in the average structure of Li_2NH over the course of this experiment. Peaks corresponding to a small Li_3N component are present throughout and are thought to originate on the outside lithium metal surface closest to the Kapton window of the cell, where visible nitriding could be seen. Supplementary Figure 15 displays a separate cell run on a further accelerated timescale (current density doubled every hour) along with cycling for 18 hours at 10 mAcm^{-2}. The lowering of resistance and stable cycling behaviour at 10 mA cm^{-2} is well demonstrated here together with no corresponding change in average structure. After a rest period (approximately 6 hours) this cell was rerun on a similar programme from 40 μA cm^{-2} up to 70 mA cm^{-2}. At the highest current densities, a large polarisation in the voltage profile of each cycle is observed along with variation in the measured diffraction signal for Li metal, but it again appears that there is no short circuit. The lack of structural variation whilst cycling excludes the possibility of a bulk phase transition of Li_2NH from $Fd\bar{3}m \rightarrow Fm\bar{3}m$. This, combined with the *ex-situ* NMR data, strengthens the hypothesis that the observed increase in ionic conductivity may be due to small-scale stoichiometry variation confined to the grain boundary.

An *in-situ* ^{7}Li NMR S&P experiment was performed to further probe this hypothesis. The electrochemical data for this experiment are displayed in Supplementary Figure 16 with a contour plot of the observed NMR spectra in Figure 4b. The spectra show a strong signal centred close to 0 ppm from Li_2NH and a smaller signal from Li metal at around 260 ppm. In this case, the cell was cycled at each current density for 3 hours then doubled, starting from 40 μA cm^{-2} up to 2.56 mA cm^{-2}. The cell was then cycled at 320 μA cm^{-2} for 12 hours before a 12-hour rest period. The electrochemical data can be observed to be noisy, possibly indicating dendrite formation although this is countered by the observed recovery of the voltage profiles. No significant change in the shift of the Li_2NH peak is observed whilst current is applied, indicating that the local Li environment within Li_2NH does not change drastically during cycling. The absence of significant shifts outside the diamagnetic region (except for Li metal itself) also confirms that the sample does not become electronically conductive.[62] The development of a small Li metal component (~267 ppm) in addition to the original Li metal signal (~263 ppm) indicates the formation of Li microstructures during cycling. The deposited Li is likely to be rough (the Li-Li_2NH interphase is quite flat)

rather than dendritic, as the latter experiences different bulk magnetic susceptibility effects, since it grows perpendicularly to the Li metal in the cell (and to the applied field), resulting in a larger shift (~10 ppm) from that of the bulk Li signal.[63]

Monitoring the variation in the integral of the Li metal and Li_2NH peaks over time (Supplementary Figure 17) reveals initially a drop in the Li-metal signal in the first hour followed by an increase in the next 14 h, this increase being consistent with some formation of Li microstructures at the Li-Li_2NH interface. A similar drop is observed in the Li_2NH signal, which then recovers as the current density is doubled from 40 μA cm^{-2} to 80 μA cm^{-2} (a decrease in the cell potential is also observed at this point). The signal then slowly decays throughout the remaining cycling period suggesting potential Li loss from the Li_2NH phase. The ^{7}Li NMR spectra corresponding to pre-cycling, at the final cycle, and after 12 h resting at zero current (Figure 4c) were fitted using a chemical shift anisotropy (CSA) static model: two components were fitted, one quasi-axial likely corresponding to Li in the interstitial sites (broader, in purple in the spectra) and one rhombic assigned to the Li in tetrahedral sites (narrow and in blue). The fits show that the broad component progressively shifts during cycling (3.40 → 3.25 ppm), with a slightly more significant shift occurring during the rest period (3.25 → 3.03 ppm), while the narrow component remains approximately constant at ~3.30 ppm.

While it is difficult to unambiguously determine the nature of the different local environments, the observed changes in chemical shift after cycling suggest that the stoichiometry of Li_2NH varies upon cycling. This may give insight into the observed changes in conductivity and resistance recovery behaviour discussed above. We hypothesise that under applied current or potential there is a stoichiometry variation at the grain boundary leading to a disordering of the surface of the Li_2NH particles and a highly conductive state, similar to that described for Li_2NH ammonia cracking catalysts.[57,64] There is likely some exchange of this highly conductive state with the bulk (reflected by the change in signal before and immediately after cycling). However, the change is metastable and when the electrochemical bias is removed the compositional gradients lessen through diffusion further into the bulk grain, as represented by the greater shift in signal after rest and resulting in the recovery in resistance observed in the EIS spectra (see Figure 4d for a schematic depiction of this process). We stress that this variation in stoichiometry is very minor and not significant enough to alter the average structure of the material and hence we do not observe this relaxation *via* diffraction. Additional surface sensitive Dynamic Nuclear Polarisation (DNP) NMR experiments could help confirm the local environment at the grain boundary.

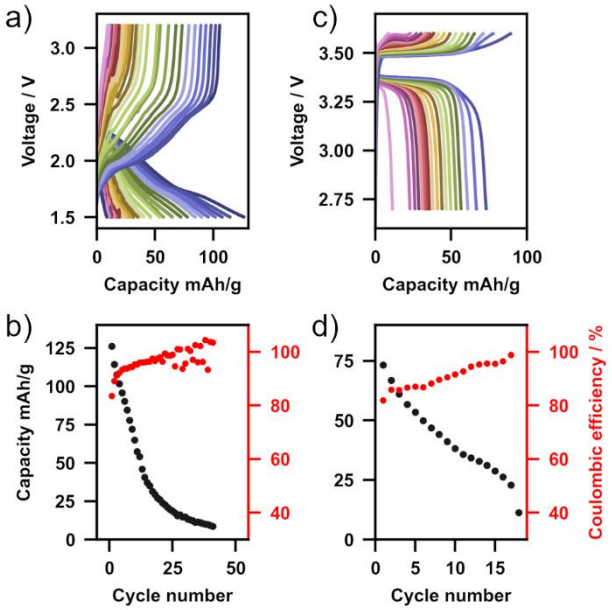

Figure 5: a) Charge-discharge cycles of a Li|Li_2NH|TiS_2 cell at 40 ˚C. b) Capacity and coulombic efficiency vs cycle number of Li|Li_2NH|TiS_2 cell. c) Charge-discharge cycles of a Li|Li_2NH|$LiFePO_4$ cell at 40 ˚C. d) Capacity and coulombic efficiency vs cycle number of Li|Li_2NH|$LiFePO_4$ cell.

As this potential stoichiometric variation occurs whilst in contact with lithium metal, it is prudent to consider any possible reactions between the two materials. Equations 1 & 2 detail possible mechanisms for stoichiometric variation.

$$(1)\ xLi + Li_2NH \rightarrow Li_{2+x}NH$$
$$(2)\ (x+1)Li_2NH \rightarrow Li_{2-x}NH_{1+x} + xLi_3N$$

Equation 1 relates to the formation of surface imide-nitride-hydride whilst equation 2 details the formation of an imide-amide phase and lithium nitride. As such, an assessment of the nature of the stoichiometry variation observed was conducted via NMR measurement of two more *ex-situ* samples: a lithium imide-amide (Li deficient compared to Li_2NH, $Li_{1.917}NH_{1.083}$) and a lithium imide-nitride-hydride ($Li_{2.083}NH$) (Supplementary Figure 18). Both of these materials also take an antifluorite-type structure and simply represent a shift in bulk stoichiometry compared to Li_2NH (See Supplementary Figure 19 for diffraction and structural data). The ^{7}Li and ^{1}H NMR spectra of these samples confirm a change in the local structure compared to pristine Li_2NH (Supplementary Figure 11). For both the imide-amide and imide-nitride-hydride, the ^{7}Li spectra contain two resonances (sharp and broad). These are centred at 2.08 ppm (sharp) and 1.56 ppm (broad) for the amide-imide and 3.36 ppm (sharp) and 3.03 ppm (broad) for the imide-nitride-hydride (we note that the linewidth of the imide-nitride-hydride is however ~ 2× that of the other samples analysed here). In both samples there is a shift to lower ppm in the broad component as compared to pristine Li_2NH. Observing the ^{7}Li spectra in isolation, the post-cycled material appears to resemble the imide-nitride-hydride most

closely, particularly considering the chemical shift of the broad component is identical (3.03 ppm). However, the ^{1}H spectra show two resonances centred at − 5.59 and − 2.74 ppm for the amide-imide and three resonances at − 4.98, 0.67 and 3.00 ppm for the imide-nitride-hydride. In this case the ^{1}H spectrum of the post-cycled sample most closely resembles the spectrum of the imide-amide: in both spectra the main component (light blue in Supplementary Figure 18) shifted to a more a negative ppm compared to pristine Li_2NH. The signal at 3.00 ppm in the imide-nitride-hydride spectrum, likely corresponding to the hydride anions, is also not observed post-cycling. Comparison to these fixed off-stoichiometry samples is therefore likely to be a simplification of the overall picture and it is possible that formation of imide-amide and imide-nitride-hydride phases are happening simultaneously during cycling. We do however note that observation of Li loss from the Li_2NH phase in our *in situ* NMR and CV experiments, suggest the change in stoichiometry is on average towards an imide-amide type phase ($Li_{2-x}NH_{1+x}$). Furthermore, it is these lithium imide-amide phases that have been computationally observed to exhibit significant surface disorder, supporting our theory for the apparent conductivity improvement.[64]

Li-metal battery cell tests

Li_2NH was evaluated for its practical application as a solid electrolyte material in Li-metal battery cells using a Li-metal anode and two different cathode materials (TiS_2 and $LiFePO_4$). In both cases a small amount of liquid electrolyte (10 µL, $LiPF_6$ in EC:DMC for TiS_2, $LiPF_6$ in EC:EMC with 2 wt% vinyl chloride for LFP) was used to wet the solid electrolyte–cathode interface forming so-called hybrid solid-state batteries. Figure 5 shows charge-discharge measurements operated at 5 mA g^{-1} for each of these cells (5a – TiS_2, 5b – LFP) as well as capacity and columbic efficiency as a function of cycle number (5c – TiS_2, 5d – LFP). With both cathode materials multiple charge-discharge cycles are observed, demonstrating the first application of Li_2NH as a functioning solid electrolyte in a full cell. With a TiS_2 cathode, over 40 cycles were completed with a relatively high initial discharge capacity of 126 mAh g^{-1}. Capacity fade was observed in both cells, with the TiS_2 cell terminating after 42 cycles and the LFP cell diminishing after 18 cycles. This cell degradation is likely from the formation of an unstable CEI layer at the Li_2NH-cathode interface due to a reaction with the liquid electrolyte, and is particularly prominent at voltages above 3.5 V, hence the worse performance of the LFP cells. This is supported by the inferior stability of LFP cells when the 2 wt% vinyl chloride additive is not used in the liquid electrolyte formulation (Supplementary Figure 18). In either case, no indication of reduction in cell impedance analogous to the S&P experiments was observed, however, it is possible that this is due to the low number of cycles in these battery cycling experiments. As this is the first demonstration of this material in operation, we anticipate that further optimisation of cell formulation both in hybrid and all-solid-state configurations will further improve performance and provide an opportunity to observe the enhanced conductivity. However, it should be noted that our current data indicate that the enhancement is metastable, and so further work should explore whether there are ways to control this effect. For example, further molecular dynamics simulations on lithium imide-based catalysts have shown that partial conversion to amide groups enhances the observed surface mobility, suggesting that there may be avenues for building this enhanced grain boundary conductivity into the design of lithium imide type SSEs through composition control.[64] At the very least, given the known ability of the antifluorite structure to incorporate amide, nitride, hydride and halides, there is significant potential for a new family of high-conductivity materials to be explored. [31,65,66]

Summary

The results reported here demonstrate the promising performance of antifluorite Li_2NH for application as a solid electrolyte in solid-state Li-ion batteries. A high initial ionic conductivity of Li_2NH is further improved through modest post-synthetic milling and hot-pressing regimes resulting in the highest reported conductivity for this material at 1 mS cm^{-1}. High current operation at up to 70 mA cm^{-2} as well as wide voltage stability (0-5 V vs Li/Li$^+$) is reported. An interaction with Li-metal electrodes is also observed, with an apparent improvement in ionic conductivity to > 10 mS cm^{-1} whilst remaining electronically insulating. This interaction is hypothesised to occur along the grain boundary of the material and may be as a result of stoichiometry variation at the Li_2NH particle surface producing a highly disordered quasi-liquid surface. The impressive performance of this material in these initial investigations suggests the potential for further enhancements. Through the level of understanding of the possible composition modifications of lithium imide in the hydrogen storage literature, a wealth of new imide-based ionic conductors are open for further investigation.

References

1. Lin, D., Liu, Y. & Cui, Y. Reviving the lithium metal anode for high-energy batteries. *Nat Nanotechnol* **12**, 194–206 (2017).
2. Xu, W. *et al.* Lithium metal anodes for rechargeable batteries. *Energy Environ Sci* **7**, 513–537 (2014).
3. Bai, P., Li, J., Brushett, F. R. & Bazant, M. Z. Transition of lithium growth mechanisms in liquid electrolytes. *Energy Environ Sci* **9**, 3221–3229 (2016).
4. Famprikis, T., Canepa, P., Dawson, J. A., Islam, M. S. & Masquelier, C. Fundamentals of inorganic

solid-state electrolytes for batteries. *Nat Mater* **18**, 1278–1291 (2019).
5. Fergus, J. W. Ceramic and polymeric solid electrolytes for lithium-ion batteries. *J Power Sources* **195**, 4554–4569 (2010).
6. Manthiram, A., Yu, X. & Wang, S. Lithium battery chemistries enabled by solid-state electrolytes. *Nat Rev Mater* **2**, 1–16 (2017).
7. Zhang, Z. *et al.* New horizons for inorganic solid state ion conductors. *Energ Environ Sci* **11**, 1945–1976 (2018).
8. Goodenough, J. B. & Kim, Y. Challenges for rechargeable Li batteries. *Chem Mater* **22**, 587–603 (2010).
9. Zhang, T., Fuchs, B., Secchiaroli, M., Wohlfahrt-Mehrens, M. & Dsoke, S. Electrochemical behavior and stability of a commercial activated carbon in various organic electrolyte combinations containing Li-salts. *Electrochim Acta* **218**, 163–173 (2016).
10. Thangadurai, V., Narayanan, S. & Pinzaru, D. Garnet-type solid-state fast Li ion conductors for Li batteries: Critical review. *Chem Soc Rev* **43**, 4714–4727 (2014).
11. Wang, C. *et al.* Garnet-Type Solid-State Electrolytes: Materials, Interfaces, and Batteries. *Chem Rev* **120**, 4257–4300 (2020).
12. Murugan, R., Thangadurai, V. & Weppner, W. Fast lithium ion conduction in garnet-type $Li_7La_3Zr_2O_{12}$. *Angew Chem Int Edit* **46**, 7778–7781 (2007).
13. Kamaya, N. *et al.* A lithium superionic conductor. *Nat Mater* **10**, 682–686 (2011).
14. Boulineau, S., Courty, M., Tarascon, J. M. & Viallet, V. Mechanochemical synthesis of Li-argyrodite Li_6PS_5X (X = Cl, Br, I) as sulfur-based solid electrolytes for all solid state batteries application. *Solid State Ion* **221**, 1–5 (2012).
15. Adeli, P. *et al.* Boosting Solid-State Diffusivity and Conductivity in Lithium Superionic Argyrodites by Halide Substitution. *Angew Chem Int Edit* **58**, 8681–8686 (2019).
16. Sharafi, A. *et al.* Impact of air exposure and surface chemistry on Li-$Li_7La_3Zr_2O_{12}$ interfacial resistance. *J Mater Chem A* **5**, 13475–13487 (2017).
17. Krauskopf, T., Hartmann, H., Zeier, W. G. & Janek, J. Toward a Fundamental Understanding of the Lithium Metal Anode in Solid-State Batteries - An Electrochemo-Mechanical Study on the Garnet-Type Solid Electrolyte $Li_{6.25}Al_{0.25}La_3Zr_2O_{12}$. *ACS Appl Mater Inter* **11**, 14463–14477 (2019).
18. Mangani, L. R. & Villevieille, C. Mechanical vs. chemical stability of sulphide-based solid-state batteries. Which one is the biggest challenge to tackle? Overview of solid-state batteries and hybrid solid state batteries. *J Mater Chem A* **8**, 10150–10167 (2020).
19. Hagenmuller, P., Réau, J. M., Lucat, C., Matar, S. & Villeneuve, G. Ionic conductivity of fluorite-type fluorides. *Solid State Ionics* **3–4**, 341–345 (1981).
20. Sorokin, N. I. & Sobolev, B. P. Nonstoichiometric fluorides-Solid electrolytes for electrochemical devices: A review. *Crystallogr Rep* **52**, 842–863 (2007).
21. Reau, J. M. & Hagenmuller, P. Fast ionic conductivity of fluorine anions with fluorite -or tysonite-type structures. *Rev Inorg Chem* **19**, 45–77 (1999).
22. Mogensen, M., Lybye, D., Bonanos, N., Hendriksen, P. V. & Poulsen, F. W. Factors controlling the oxide ion conductivity of fluorite and perovskite structured oxides. *Solid State Ionics* **174**, 279–286 (2004).
23. Molaiyan, P. & Witter, R. Crystal phase and surface defect driven synthesis of $Pb_{1-x}Sn_xF_2$ solid solution electrolyte for fluoride ion batteries. *J Electroanal Chem* **845**, 154–159 (2019).
24. Szczuka, C. *et al.* Forced Disorder in the Solid Solution Li_3P-Li_2S: A New Class of Fully Reduced Solid Electrolytes for Lithium Metal Anodes. *J Am Chem Soc* **144**, 16350–16365 (2022).
25. Li, W. *et al.* Lithium-compatible and air-stable vacancy-rich $Li_9N_2Cl_3$ for high-areal capacity, long-cycling all-solid-state lithium metal batteries. *Sci Adv* **9**, eadh4626 (2023).
26. Landgraf, V. *et al.* Li_5NCl_2: A Fully-Reduced, Highly-Disordered Nitride-Halide Electrolyte for Solid-State Batteries with Lithium-Metal Anodes. *ACS Appl Energy Mater* **6**, 1661–1672 (2023).
27. Ping, C., Zhitao, X., Jizhong, L., Jianyi, L. & Kuang Lee, T. Interaction of hydrogen with metal nitrides and imides. *Nature* **420**, 20–22 (2002).
28. Herbst, J. F. & Hector, L. G. Energetics of the Li amide/Li imide hydrogen storage reaction. *Phys Rev B* **72**, 2–9 (2005).
29. Makepeace, J. W., Wood, T. J., Hunter, H. M. A., Jones, M. O. & David, W. I. F. Ammonia decomposition catalysis using non-stoichiometric lithium imide. *Chem Sci* **6**, 3805–3815 (2015).
30. Brooker-Davis, C. A., Makepeace, J. W. & Wood, T. J. Enhancement of the Catalytic Activity of Lithium Amide towards Ammonia Decomposition by Addition of Transition Metals. *The Journal of Ammonia Energy* **01**, 46-58 (2023).
31. Makepeace, J. W. *et al.* Compositional flexibility in Li-N-H materials: implications for ammonia catalysis and hydrogen storage. *Phys Chem Chem Phys* **23**, 15091–15100 (2021).
32. Boukamp, B. A. & Huggins, R. A. Ionic conductivity in lithium imide. *Phys Lett A* **72**, 464–466 (1979).
33. Li, W., Wu, G., Xiong, Z., Feng, Y. P. & Chen, P. Li + ionic conductivities and diffusion mechanisms in Li-based imides and lithium amide. *Phys Chem Chem Phys* **14**, 1596–1606 (2012).
34. Paik, B. & Wolczyk, A. Lithium Imide (Li_2NH) as a Solid-State Electrolyte for Electrochemical Energy Storage Applications. *J Phys Chem C* **123**, 1619–1625 (2019).
35. Zhang, J. & Hu, Y. H. Promoter effect of Cl- anion on decomposition of lithium amide and lithium imide. *ACS National Meeting Book of Abstracts* 8058–8064 (2011).

36. Haigh, P. J., Forman, R. A. & Frisch, R. C. Nuclear magnetic resonance of 7Li and 1H in solid lithium imide, lithium amide, and lithium nitride. *J Chem Phys* **45**, 812–816 (1966).
37. Mueller, T. & Ceder, G. Ab initio study of the low-temperature phases of lithium imide. *Phys Rev B* **82**, 1–7 (2010).
38. Miceli, G., Ceriotti, M., Angioletti-Uberti, S., Bernasconi, M. & Parrinello, M. First-principles study of the high-temperature phase of Li_2NH. *J Phys Chem C* **115**, 7076–7080 (2011).
39. Hu, Y. H. & Ruckenstein, E. Ultrafast reaction between Li_3N and $LiNH_2$ to prepare the effective hydrogen storage material Li_2NH. *Ind Eng Chem Res* **45**, 4993–4998 (2006).
40. Ichikawa, T. & Isobe, S. The structural properties of amides and imides as hydrogen storage materials. *Z Kristallog* **223**, 660–665 (2008).
41. Noritake, T. *et al.* Crystal structure and charge density analysis of Li_2NH by synchrotron X-ray diffraction. *J Alloy Compd* **393**, 264–268 (2005).
42. Ohoyama, K., Nakamori, Y., Orimo, S. I. & Yamada, K. Revised crystal structure model of Li_2NH by neutron powder diffraction. *J Phys Soc Japan* **74**, 483–487 (2005).
43. Balogh, M. P., Jones, C. Y., Herbst, J. F., Hector, L. G. & Kundrat, M. Crystal structures and phase transformation of deuterated lithium imide, Li_2ND. *J Alloy Compd* **420**, 326–336 (2006).
44. David, W. I. F. *et al.* A mechanism for non-stoichiometry in the lithium amide/lithium imide hydrogen storage reaction. *J Am Chem Soc* **129**, 1594–1601 (2007).
45. Makepeace, J. W. & David, W. I. F. Structural Insights into the Lithium Amide-Imide Solid Solution. *J of Phys Chem C* **121**, 12010–12017 (2017).
46. Tapia-Ruiz, N., Sorbie, N., Vaché, N., Hoang, T. K. A. & Gregory, D. H. Rapid microwave synthesis, characterization and reactivity of lithium nitride hydride, Li_4NH. *Materials* **6**, 5410–5426 (2013).
47. Kravchenko, N. G., Zhdanov, V. V., Kaizer, E. B. & Poplavnoi, A. S. First Principles Investigations of the Crystal Structure, Electron Spectra, and Chemical Bonding in the Low-Temperature Phase of Lithium Imide. *J Struct Chem+* **59**, 1258–1264 (2018).
48. Bonnet, M. L., Iannuzzi, M., Sebastiani, D. & Hutter, J. Local disorder in lithium imide from density functional simulation and NMR spectroscopy. *J Phys Chem C* **116**, 18577–18583 (2012).
49. Miceli, G., Ceriotti, M., Bernasconi, M. & Parrinello, M. Static disorder and structural correlations in the low-temperature phase of lithium imide. *Phys Rev B* **83**, 2–6 (2011).
50. Araújo, C. M., Blomqvist, A., Scheicher, R. H., Chen, P. & Ahuja, R. Superionicity in the hydrogen storage material Li_2NH: Molecular dynamics simulations. *Phys Rev B* **79**, 1–4 (2009).
51. Kojima, Y. & Kawai, Y. IR characterizations of lithium imide and amide. *J Alloy Compd* **395**, 236–239 (2005).
52. Ramakumar, S., Deviannapoorani, C., Dhivya, L., Shankar, L. S. & Murugan, R. Lithium garnets: Synthesis, structure, Li+ conductivity, Li+ dynamics and applications. *Prog Mater Sci* **88**, 325–411 (2017).
53. Rongeat, C., Reddy, M. A., Witter, R. & Fichtner, M. Nanostructured fluorite-type fluorides as electrolytes for fluoride ion batteries. *J Phys Chem C* **117**, 4943–4950 (2013).
54. Grinderslev, J. B. *et al.* Methylamine Lithium Borohydride as Electrolyte for All-Solid-State Batteries. *Angew Chem Int Edit* **61**, 1–7 (2022).
55. Wang, Z., Ye, Z., Zhang, Y., Li, C. & Zeng, Y. Fluorite-doped $Gd_{0.1}Ce_{0.9}O_{1.95}$ polycrystalline electrolytes with extraordinarily enhanced oxide ionic conductivities controlled by depletion degree of oxygen vacancies at grain boundaries. *J Power Sources* **480**, 229118 (2020).
56. Chen, I. W. Grain boundary kinetics in oxide ceramics with the cubic fluorite crystal structure and its derivatives. *Interface Sci* **8**, 147–156 (2000).
57. Yang, M., Raucci, U. & Parrinello, M. Reactant-Induced Dynamics of Lithium Imide Surfaces during the Ammonia Decomposition Process. *Nat Catal* 6, 829–836 (2023).
58. Lazanas, A. C. & Prodromidis, M. I. Electrochemical Impedance Spectroscopy─A Tutorial. *ACS Meas Sci Au* **3**, 162–193 (2023).
59. Taibl, S., Fafilek, G. & Fleig, J. Impedance spectra of Fe-doped $SrTiO_3$ thin films upon bias voltage: Inductive loops as a trace of ion motion. *Nanoscale* **8**, 13954–13966 (2016).
60. West, A., Irvine, J. & Sinclair, D. Electroceramics: Characterization by Impedance Spectroscopy. *Adv Mater* **2**, 132–138 (1990).
61. Hayashi, K., Sushko, P. V., Hashimoto, Y., Shluger, A. L. & Hosono, H. Hydride ions in oxide hosts hidden by hydroxide ions. *Nat Commun* **5**, 1–8 (2014).
62. Knight, W. D. Nuclear Magnetic Resonance Shift in Metals. *Phys Rev* **76**, 1259 (1949).
63. Chang, H. J. *et al.* Investigating Li Microstructure Formation on Li Anodes for Lithium Batteries by in Situ 6Li/7Li NMR and SEM. *J Phys Chem C* **119**, 16443–16451 (2015).
64. Mambretti, F., Raucci, U., Yang, M. & Parrinello, M. How Does Structural Disorder Impact Heterogeneous Catalysts? The Case of Ammonia Decomposition on Non-Stoichiometric Lithium Imide. *ACS Catal* **14**, 1252–1256 (2024)
65. Anderson, P. A., Chater, P. A., Hewett, D. R. & Slater, P. R. Hydrogen storage and ionic mobility in amide-halide systems. *Faraday Discuss* **151**, 271–284 (2011).
66. Lefevour, P. E. F. United States Patent (19). 0–5 (1983).

67. Coelho, A. TOPAS and TOPAS-Academic: An optimization program integrating computer algebra and crystallographic objects written in C++. *J. Appl Cryst* **51**, 210–218 (2018)
68. Pecher, O., Carretero-Gonzalez, J., Griffith, K. J. & Grey, C. P. Materials' methods: NMR in battery research. *Chem Mater* **29**, 213–242 (2017).
69. Massiot, D. *et al.* Modelling one- and two-dimensional solid-state NMR spectra. *Magn Reson Chem* **40**, 70–76 (2002).
70. Inaguma, Y., Liquan, C., Itoh, M. & Nakamura, T. High Ionic Conductivity in Lithium Lanthanum Titanate. *Solid State Commun* **86**, 689–693 (1993).
71. Hebb, M. Electrical conductivity of silver sulfide. *J. Chem. Phys.*, **20**, 185–190 (1952).

Methods:

Sample handing. All sample handing was performed in an argon filled glovebox (MBraun, Unilab, < 0.1ppm H_2O, < 0.1ppm O_2).

Synthesis. Synthesis of Li_2NH was achieved by the solid-state reaction of $LiNH_2$ (Sigma Aldrich hydrogen storage grade) with Li_3N (Sigma Aldrich >99.5%) in stoichiometric quantities.

$$Li_3N + LiNH_2 \rightarrow 2Li_2NH$$

The reagents were weighed out in order to form 1 g of Li_2NH (0.3973 g $LiNH_2$ and 0.6027 g Li_3N). Samples were first hand-ground using an agate pestle and mortar for 2 minutes before being transferred into a Si_3N_4 milling jar (volume 45 ml) prefilled with 20 g of 5mm diameter Si_3N_4 milling balls. The jar was sealed and transferred from the glovebox to a Fritsch Pulverisette 7 Premium Line planetary micro mill. The mixture was milled at a rate of 150 rpm for 1 hour. Once returned to the glovebox the resultant mixture was transferred into a quartz tube and fitted with a Young's tap T-piece connected by an Ultra-Torr fitting. This reaction vessel was then clamped into a tube furnace (Lenton Furnaces, LTF 12/25/250 fitted with a Eurotherm 3216P1 controller) and gas lines were attached either side of the Young's tap. Argon gas was then allowed to flow through the tap. The furnace was ramped to 325 °C at a rate of 2 °C min^{-1} and held at that temperature for 12 hours. The sample of $Li_{1.917}NH_{1.083}$ was synthesised by varying the Li_3N to $LiNH_2$ ratio to give the appropriate stoichiometry.

For the lithium imide-nitride-hydride sample ($Li_{2.083}NH$), lithium nitride hydride was synthesised by the reaction of lithium nitride with lithium hydride (Sigma Aldrich, 98%) according to the following reaction:

$$Li_3N + LiH \rightarrow Li_4NH$$

The powder mixture was milled as above, pressed into a pellet and then heated in a microwave reactor (CEM Discover) for five rounds of 1-minute heating at 300W under argon flow. The synthesised lithium nitride hydride was then mixed with lithium imide, milled as above and heated to 540 °C under flowing argon for 12 hours (2 ˚C/min ramp rate):

$$0.083*Li_4NH + 1.917*Li_2NH \rightarrow 2Li_{2.083}NH$$

X-ray diffraction. Laboratory powder X-ray diffraction (XRD) measurements were carried out using a Stoe Stadi-P instrument (Mo $K_{\alpha 1}$ source) with samples sealed in capillaries made from Cole-Parmer polyimide tubing (0.7 mm internal diameter). Rietveld analysis of XRD patterns was performed using TOPAS Academic software.[67]

Raman spectroscopy. Raman measurements were taken using Renishaw InVia Raman microscope. Samples were loaded in a borosilicate glass capillary (0.7 mm internal diameter) to an approximate height of 5 mm and sealed with vacuum grease. A laser wavelength of 532 nm was used to analyse the samples. Spectra were taken in the region of 3000 cm^{-1} to 3400 cm^{-1} using a laser power of 0.5% and a typical exposure time of 10 seconds.

Preparation of Li_2NH for electrochemical measurements. The Li_2NH powder was pressed into a pellet (diameter 10 mm, thickness 1-2 mm) under an Ar atmosphere. For Au|Li_2NH|Au cells, a small amount of vacuum grease was applied to the curved side edge of each pellet before both sides were sputtered with gold using an Agar auto sputter coater placed inside an argon filled glove bag. Sputtered pellets were returned to a glovebox and the gold and grease were removed from the sides to leave gold electrodes only on the faces of each pellet. For Li|Li_2NH|Li cells, lithium foil (Pi-KEM) was cut into 10mm circles using a hole punch and any surface oxidation was removed using a spatula. The Li foil was then applied to both sides of the pellet and light pressure was applied by hand. For Li|Li_2NH|Steel cells the Li metal was only applied to one side of the pellet. In all cases, each cell was constructed into coin cells for all electrochemical measurements. Coin cell assembly took place by placing each pellet with attached electrodes in a CR2032 cell cap. A stainless-steel spacer (0.5 mm thickness) and spring (0.25 mm thickness) were placed on top followed by a CR2032 cell cap with an attached O-ring. The cell was then sealed using a Hohsen Corp coin cell crimper. Stabilisation of the Li-Li_2NH interface was conducted on already constructed coin cells by placing cells in an oven (Memmert, UN55) at 60-80 ˚C for 6-8 hours.

Electrochemical impedance spectroscopy. Variable temperature electrochemical impedance spectroscopy measurements were taken in a Carbolite VST 12/400 tube furnace heated to a maximum of 110 ˚C, with the impedance measurements (100 mV perturbation) being taken by a Hewlett Packard 4192A LF between

frequencies of 5Hz to 13MHz. Measurements on Li|Li_2NH|Li cells were taken using a Solartron 1260 impedance analyser (100 mV perturbation) from 1 mHz to 10 MHz. Impedance data were analysed using Zview software by Scribner. In general, resistance values for Li_2NH were taken as the high intercept of the first semi-circle. Where data were fitted to equivalent circuit models, resistance of the material was taken as the combined resistance of R1 and R2 (See Supplementary Figure 1 and Supplementary Table 1). Area specific resistance was calculated by normalising Li|Li_2NH|Li data to the surface area of the pellet (0.7854 cm^2) and dividing the calculated resistance by 2 to account for the two Li electrodes. For Figure 3d (Supplementary Figure 7) the resistance was taken as the high intercept of the assumed semi-circle (approximately 61 Ω cm).

DC polarisation. Electronic conductivity of Li_2NH was evaluated using DC polarisation experiments. Different voltages (0.5 V & 0.75 V) were applied for a period of 5 hours on an Au|Li_2NH|Au cell held at 40 ˚C using a Biologic VMP3. The electronic conductivity was calculated using the following equation:

$$(3)\ \sigma_e = \frac{L}{A} \times \frac{I_f}{V}$$

Where L is the thickness of the pellet, A is the surface area of the pellet, V is the applied potential, and I_f refers to the average current of the last half hour of the relaxation period. Transference numbers were calculated from the voltage vs time plots using the following equations:

$$(4)\ t_e = \frac{I_f}{I_t}$$

$$(5)\ t_i = 1 - t_e$$

Where t_e and t_i are the electronic and ionic transference numbers respectively and I_t is the initial current upon polarisation.

Cyclic Voltammetry. Cyclic voltammetry was conducted on Li|Li_2NH|Steel cells held at 40 ˚C using a Biologic VMP3 across a range of voltages from -0.5 V up to 5 V vs Li/Li^+ at a scan rate of 1 mV s^{-1}. Electronic conductivity was evaluated both before and immediately after the CV experiment using the Hebb-Wagner method.[71] The same cell had a 0.5 V potential applied for 5 hours and the current response measured. The electronic conductivity was calculated as per Equation 3. Transference numbers were calculated as per Equations 4 & 5.

Lithium stripping and plating. Lithium stripping and plating experiments were conducted on symmetrical Li|Li_2NH|Li coin cells held at 40 ˚C using a Biologic VMP3. These symmetric cells were cycled under constant current conditions at various current densities for 15 minutes plus a 10s rest per half cycle making each full cycle approximately 30 minutes long.

Synchrotron X-ray powder diffraction. Where appropriate, synchrotron measurements were undertaken on the I11 beamline at Diamond Light Source, with powder samples sealed in 0.5 mm borosilicate capillaries. Lithium stripping and plating experiments were conducted on modified Li|Li_2NH|Li coin cells with a 3 mm diameter Kapton window to allow for beam penetration. These cells were cycled under identical conditions to the stripping and plating experiments except on an accelerated timescale and using an Ivium Octostat potentiostat. Diffraction data (λ=0.824042 Å) were collected on each of the two cycling cells every 100s using position sensitive detectors (PSD), with 10s total collection time per scan. The cells were aligned in the beam relative to the diffraction pattern of a 0.5 mm borosilicate capillary measurement of lithium imide.

Solid State NMR. Solid-state Nuclear Magnetic Resonance (NMR) experiments were performed on the pristine Li_2NH powder as synthesized, after cycling (*ex situ*) and *in situ* during electrochemical cycling. *Ex situ* solid state NMR spectra on the pristine material and $Li_{1.917}NH_{1.083}$ were acquired on a 11.7 T (ω_H = 500 MHz) Bruker Avance III spectrometer, while the cycled Li_2NH spectra were acquired on a 16.4 T (ω_H = 700 MHz) Bruker Avance III spectrometer. In both cases a Bruker 1.3 mm magic angle spinning (MAS) probe was used with a MAS frequency of 40 kHz. The spectra were externally referenced to glycine (spun at 20 kHz) at 8.00 ppm (δ ^1H) and Li_2CO_3 at 0.00 ppm (δ ^7Li). In all cases, a rotor-synchronised Hahn-echo pulse sequence (90°–τ–180°–τ–acquire) was used for quantitative measurements. The recycle delay adopted was at least $5\times T_1$, the T_1 having been measured via a saturation recovery pulse sequence ($(sat)_n$–τ–90°–acquire). For ^7Li NMR, pulse lengths of 1.0 μs (at 11.7 T) and 2.05 μs (at 16.4 T) and recycle delays of 1.36 s (pristine), 10 s (cycled), 2.65 s ($Li_{1.917}NH_{1.083}$) were set; for ^1H NMR, pulse lengths of 0.87 μs (at 11.7 T) and 2.15 μs (at 16.4 T) and recycle delays of 28.9 s (pristine), 23.4 s (cycled) and 26.5 s ($Li_{1.917}NH_{1.083}$) were set. All spectra were scaled according to the mass of the sample and number of residuals recorded.

In situ NMR experiments were conducted on a 7.05 T (ω_H = 300 MHz) Bruker Avance NMR spectrometer equipped with an *in-situ* NMR probe (NMR Service GmbH) with automatic tuning and matching capabilities and built-in highly shielded electrochemistry connections. Additional radiofrequency low-pass filters were used on the connection to the potentiostat to prevent interference. A 12 mm inner diameter solenoid coil was used and the cell (made of polyether ether ketone, PEEK) was oriented so that the lithium chips and the electrolyte pellet were parallel to the main magnetic field.[68] During cycling, NMR spectra were recorded continuously using a one pulse sequence with a pulse length of 5.6 μs and a recycle delay of 1 s,

quantitative for Li metal and providing enough signal and time resolution for the solid electrolyte. The time resolution was of ~ 1 min per spectrum. The spectra were externally referenced to LiCl (aq) at 0.00 ppm.

All spectra were recorded and processed using Bruker Topspin 2.1, 3.6.2 and 3.6.4, fitted using DMfit software using the Chemical Shift Anisotropy (CSA) MAS/static model and analysed and plotted using home-written MATLAB scripts.[69]

Charge-discharge measurements. Charge-discharge measurements were undertaken using a Biologic VMP3 cell tester with the cells held at 40 °C, cells were rested for at least 24 hr prior to cycling. To assemble $Li|Li_2NH|LiFePO_4$ cells, Li metal was first applied to one side of a cold pressed pellet (10 mm diameter, 1.2 mm thickness) before being clamped on a hot plate and held at 60 °C for 1 hour followed by 180 °C for 2 hours. Once cooled, the pellet would be placed in a CR2032 cell cap and 10 µL of 1M $LiPF_6$ in EC:DMC with 2 wt% vinyl chloride (1:1, Sigma Aldrich) was added dropwise to the surface of the pellet. Commercially purchased $LiFePO_4$ electrode sheets (Pi-KEM) with an active loading of 7.44 mg cm^{-2} (cut into 12 mm disks) were placed onto the stack with a steel spacer (0.5 mm thickness) and spring (0.25 mm thickness) followed by a CR2032 cell cap with an attached O-ring. The cell was then sealed using a Hohsen Corp coin cell crimper.

For $Li|Li_2NH|TiS_2$ cells, a cathode slurry was prepared by mixing 80 wt% TiS_2 (99.9%, Sigma Aldrich, ball milled at 200pm for 1 hour) as an active material, 8 wt% polyvinylidene fluoride (PVDF 5130, Solvay) as a binder and 12 wt% carbon black (TimCal, C65) as a conducting additive with N-methyl-2-pyrrolidone (NMP) as the solvent in a THINKY mixer at 2000 rpm for 15 minutes . The slurry was coated uniformly on aluminium foil using the doctor blade coating technique and dried in a vacuum oven at 120 °C for 24 h. The electrodes were cut into 12 mm disks for further use. The active material loading of the cathode was maintained at 3 mg/cm^2. A cold-pressed Li_2NH pellet of 10 mm diameter and 1.2 mm thickness was used as the SSE. Li metal was used as an anode and was melded on one side of the pellet as described above. 10 µL of 1M $LiPF_6$ in EC/EMC (1:1) liquid electrolyte was again added while assembling the coin cells. The cells were discharged and charged at a current density of 5mA/g, cycling between 1.5V and 3.2V.

Acknowledgements.

JWM acknowledges a Future Leaders Fellowship (MR/S03403X/1). JPL and MPS acknowledge the University of Birmingham for studentship funding. PRS acknowledges the EPSRC grant (GENESIS project: EP/R024006/1), and the Faraday Institution CATMAT grant (FIRG016 & FIRG063) for funding. T.I. and C.P.G. were supported by an ERC Advanced Investigator Grant for C.P.G. (EC H2020 835073). Diamond Light Source is acknowledged for the provision of beamtime (CY35016), and Stephen Thompson is acknowledged for support during this experiment. Ezri McGarrigle is acknowledged for assistance with the schematic diagram (Figure 4d). Josh Deakin and Louise Male are acknowledged for support with the laboratory powder diffraction and Raman equipment.

Author Contributions. JWM and JPL conceived the study and analysed the data. JPL conducted the experiments. PAA, PRS and EMK assisted with electrochemical data interpretation and experiment design. TVB collected and analysed the TiS_2 cell data. TI and CPG designed experiments and analysed data from the solid-state NMR spectroscopy. SD assisted with collection of synchrotron X-ray diffraction data. MPS and BD assisted with the electrochemical experiments and associated analysis. JWM and JPL prepared the manuscript with input from all authors.

Competing Interests. The authors declare no competing interests.

Additional Information. Supplementary Information is available for this paper. Correspondence and requests for materials should be addressed to Dr Joshua Makepeace (j.w.makepeace@bham.ac.uk)